

Three-dimensional imaging of magnetic fields with polarized neutrons

NIKOLAY KARDJILOV^{1*}, INGO MANKE^{1,2}, MARKUS STROBL^{1,3}, ANDRÉ HILGER¹, WOLFGANG TREIMER^{1,4},
MICHAEL MEISSNER¹, THOMAS KRIST¹ AND JOHN BANHART^{1,2}

¹Hahn–Meitner Institute (HMI) Berlin, 14109 Berlin, Germany

²Berlin Institute of Technology, 10623 Berlin, Germany

³Ruprecht Karls University Heidelberg, 69120 Heidelberg, Germany

⁴University of Applied Sciences (TFH) Berlin, 13353 Berlin, Germany

*e-mail: kardjilov@hmi.de

Published online: 30 March 2008; doi:10.1038/nphys912

Neutrons are highly sensitive to magnetic fields owing to their magnetic moment, whereas their charge neutrality enables them to penetrate even massive samples. The combination of these properties with radiographic and tomographic imaging^{1–4} enables a technique that is unique for investigations of macroscopic magnetic phenomena inside solid materials. Here, we introduce a new experimental method yielding two- and three-dimensional images that represent changes of the quantum-mechanical spin state of neutrons caused by magnetic fields in and around bulk objects. It opens up a way to the detection and imaging of previously inaccessible magnetic field distributions, hence closing the gap between high-resolution two-dimensional techniques for surface magnetism^{5,6} and scattering techniques for the investigation of bulk magnetism^{7–9}. The technique was used to investigate quantum effects inside a massive sample of lead (a type-I superconductor).

The specific interaction of neutrons with matter enables neutron radiography to complement X-ray imaging methods for analysing materials¹. Conventional radiography is a geometrical projection technique based on the attenuation of a beam by a sample along a given ray. Quantum mechanically, neutrons are described by de Broglie wave packets¹⁰ whose spatial extent may be large enough to produce interference effects similar to those known from visible laser light or highly brilliant synchrotron X-rays. Measurements of the neutron wave packet's phase shift induced by the interaction with matter have a long and distinguished history^{11–14} and were recently combined with neutron imaging approaches, where two- and three-dimensionally resolved spatial information about the quantum mechanical interactions of neutrons with matter was obtained^{2,3,15}. In addition, neutrons, which from the particle-physicist's point of view are small massive particles with a confinement radius of about 0.7 fm, possess another outstanding property: a magnetic moment μ ($\mu = -9.66 \times 10^{-27} \text{ J T}^{-1}$). The magnetic moment is antiparallel to the internal angular momentum of the neutron described by a spin \mathbf{S} with the quantum number $s = 1/2$. Consequently, the high sensitivity of neutrons to magnetic interactions has extensively been and is still being exploited in numerous experiments to study fundamental magnetic properties and to understand basic phenomena in condensed matter^{7–9}.

Here, we present an experimental method that combines spin analysis with neutron imaging and yields a new contrast

mechanism for neutron radiography that enables two- and three-dimensional investigations of magnetic fields in matter. This method is unique not only in that it provides spatial information about the interaction of the spin with magnetic fields but also in its ability to measure these fields within the bulk of materials, which is not possible by any other conventional technique.

Our concept is based on the fact that any spin wavefunction corresponds to a definite spin direction and by using the Schrödinger equation we can keep track of the change of the spin direction during passage through an arbitrary inhomogeneous magnetic field. The equation of motion of the vector $\mathbf{S}(t) = (S_x(t), S_y(t), S_z(t))$ in a magnetic field $\mathbf{B}(t)$ is known to be¹⁶

$$\frac{d}{dt} S_\alpha(t) = \frac{g\mu_N}{\hbar} [\mathbf{S}(t) \times \mathbf{B}(t)]_\alpha, \quad \alpha = x, y, z,$$

where $g = -3.826$ is the g -factor for neutrons and μ_N is the nuclear magneton. It can be shown that an ensemble of polarized particles with a magnetic moment and spin $1/2$ behaves exactly like a classical magnetic moment¹⁷.

Thus, in a magnetic field, the spin component of neutrons polarized perpendicular to the field will undergo a Larmor precession according to the above equation with a frequency of

$$\omega_L = \frac{g\mu_N}{\hbar} B = \gamma_L B,$$

where γ_L is the gyromagnetic ratio of the neutron ($-1.8324 \times 10^8 \text{ rad s}^{-1} \text{ T}^{-1}$) and $B = |\mathbf{B}|$.

The fundamental idea of the method presented here is to analyse the spin states in a beam after interaction with the sample for each pixel of an imaging detector and to determine spatially resolved information about the spin rotation induced by the magnetic field of the sample^{4,18,19}. The precession angle φ for a neutron traversing a magnetic field can be written as a path integral

$$\varphi = \omega_L t = \frac{\gamma_L}{v} \int_{\text{path}} B ds,$$

where v is the velocity of the neutron. As the spin precession in a magnetic field depends on the flight time in the field, the incident polarized beam has to be monochromatic (that is, has to contain neutrons with a single velocity v). In our case, the beam

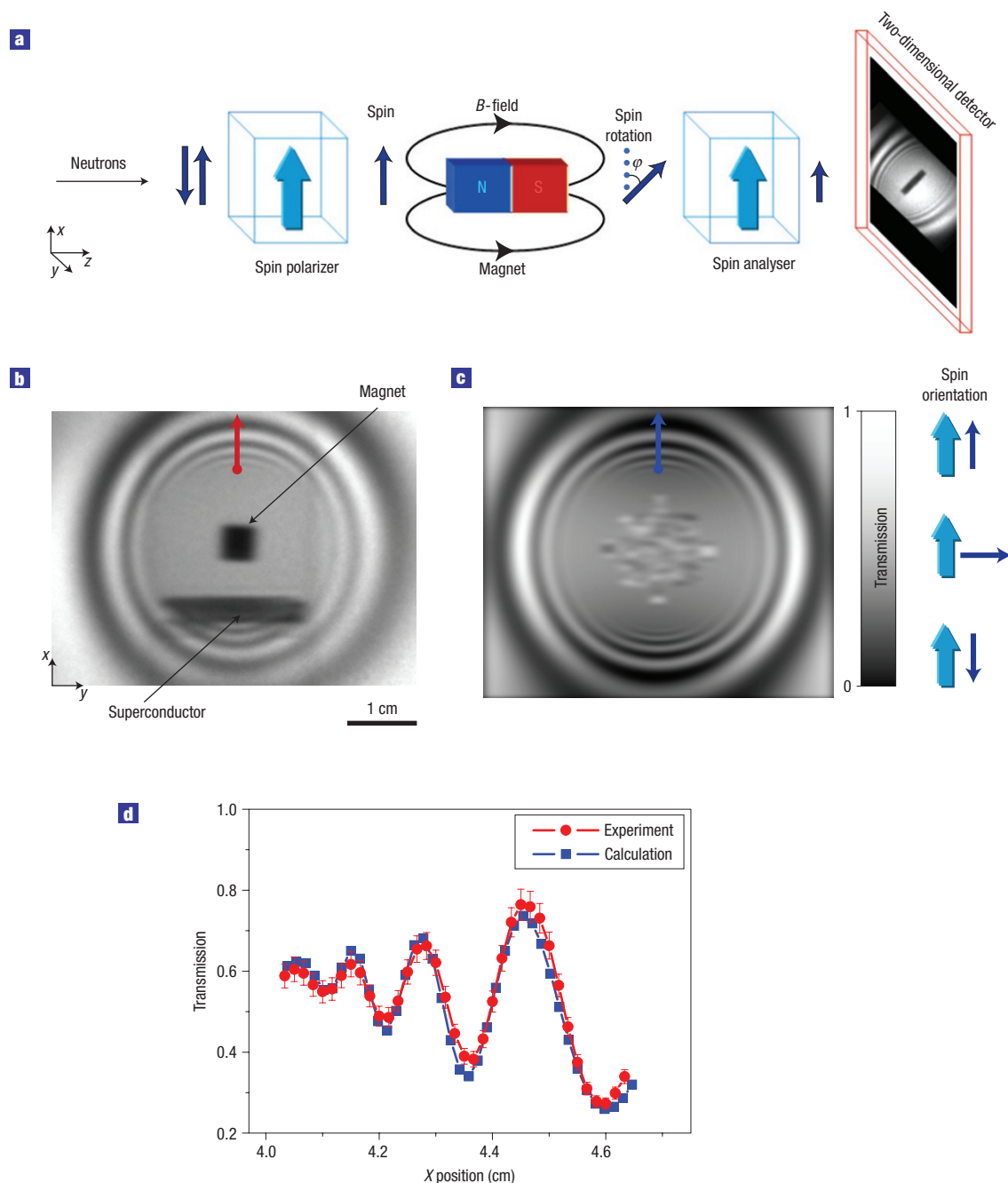


Figure 1 Spin-polarized neutron imaging. **a**, The neutron spin rotates in the magnetic field of a sample and hence typically approaches the spin analyser in a non-parallel orientation. The angle of the final spin rotation φ depends on the magnetic field along the neutron path. Changes in the polarization alter the transmission through the polarization analyser, which is indicated by a shorter arrow behind the analyser. **b**, Radiogram of a permanent magnet levitating over a $\text{YBa}_2\text{Cu}_3\text{O}_7$ superconductor obtained with spin-polarized neutrons. The field of the magnet was orientated as shown in **a**. **c**, Image simulated by using the procedure described in the Methods section. The artefact in the central part of the image is discussed in Supplementary Information, Fig. S3b. **d**, Line profiles along the coloured arrows in **b,c** were used for comparison.

was monochromatized by a double reflection using two graphite crystals as the monochromator.

The experimental set-up shown in Fig. 1a contains two polarizers²⁰, one of which is situated in front of the sample position to define the vertical beam polarization for the incident beam. The second polarizer called the (polarization) analyser in the following is located between the sample position and the imaging detector. The analyser is aligned parallel to the polarizer to guarantee the passage of neutrons carrying a spin parallel to the initial

polarization and to absorb neutrons with antiparallel spin. The image of a sample detected behind the polarization analyser is determined by a superposition of conventional attenuation contrast $I_a(x, y)$ and the contrast variations due to spin rotation $I_m(x, y)$

$$I(x, y) = \underbrace{I_0(x, y) \cdot \exp\left(-\int_{\text{path}} \Sigma(s) ds\right)}_{I_a(x, y)} \cdot \underbrace{\frac{1}{2}(1 + \cos\varphi(x, y))}_{I_m(x, y)}, \quad (1)$$

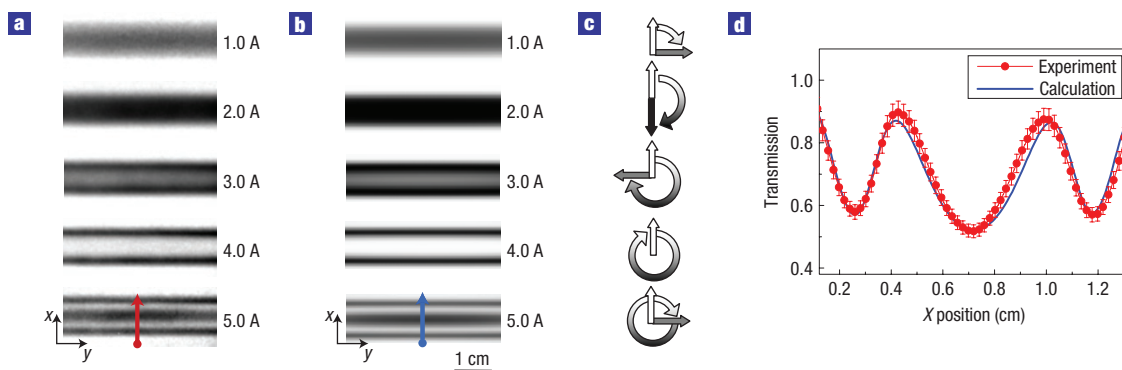


Figure 2 Comparison of experimental and calculated images obtained by polarized neutron radiography of a cylindrical coil driven with various currents.

a, Experimental results for five different currents. The grey scale represents the neutron spin rotation due to the magnetic field. **b**, Calculated images using Biot–Savart’s law. **c**, Schematic representation of the neutron spin rotation in the image centre. **d**, Line profiles along the coloured arrows in **a**, **b** for a current of 5 A. The deviation between calculation and measurement is less than 3%.

where $I_0(x, y)$ is the incident beam intensity, Σ is the linear attenuation coefficient of the sample and (x, y) are the coordinates in the detector plane. The cosine implies a periodic transmission function for the analysed precession angles (examples for different configurations of permanent magnets are shown in Supplementary Information, Fig. S1) and complicates a straightforward quantification with respect to the traversed magnetic fields. However, in many cases reverse approaches starting from an initial guess for the field distribution on the basis of known symmetries, boundary conditions or reference values can be used for quantitative image analyses. Figures 1 and 2 give examples of how precisely the images can be calculated. For more complex field configurations, iteration procedures help to derive the field distribution from experimental image data. In some other cases of irregular field distributions and for three-dimensional vector-field reconstructions, three separate measurements of different polarization orientations are indispensable^{18,19}.

The experimental arrangement shown in Fig. 1a was used for recording the radiographic projection image of a dipole magnet levitating above a superconducting $\text{YBa}_2\text{Cu}_3\text{O}_7$ pellet cooled down to 60 K (below its critical temperature $T_c = 90$ K) due to the Meissner effect (see Supplementary Information, Fig. S2 and Movie S1 for examples). The result shown in Fig. 1b illustrates the decay of the magnetic field strength with increasing distance from the magnet, resulting in an annular structure around the sample with an increasing period due to the varying precession angles of the neutron spins on their paths through the decaying field. The spatial resolution limit of the set-up (see the Methods section) is the reason why the annular structure cannot be resolved around the centre of the image. With respect to the regular structure of the magnetic field, the dipole has been oriented parallel to the beam direction. The three-dimensional field of a dipole and the corresponding spin rotation according to the measurement can be calculated, Fig. 1c (see Supplementary Information, Fig. S3a,b, for details). Comparing the measurement with the calculated data in Fig. 1d, an experimental error of about 3% can be determined, which is most likely caused by the limited precision of the energy selection and the dipole orientation with respect to the beam.

Figure 2 shows a quantitative comparison between radiographic images of an electric coil serving as an adjustable reference sample and images calculated by using Biot–Savart’s law. The coil, 88 windings of aluminium wire (1 mm) wound on an aluminium rod with 10 mm diameter and a length of 108 mm, was

placed perpendicular to the incident beam between the polarizer and the analyser. The current was varied from 0 A up to 5 A in steps of 0.1 A, and for each step an image was recorded. The measured magnetic field in the centre of the coil was 1.0 mT for an applied current of 1 A. A reference image of the field-free sample, representing $I_a(x, y)$, was recorded and used to normalize the images by calculating the ratio $I(x, y)/I_a(x, y)$. In this way, information about the changes of the spin states, that is spin rotation, was extracted. These values (Fig. 2a) are compared with data derived from the calculated local magnetic field strength (Fig. 2b) and agree well with each other (see Supplementary Information, Fig. S4 and Movie S2 for more examples).

The technique was also applied to study flux-trapping effects^{21–23} in lead—a type-I superconductor. The sample, a polycrystalline lead cylinder, was cooled down to $T_0 = 6.8$ K (below its critical temperature for superconductivity, $T_c = 7.2$ K). During cooling, a homogeneous magnetic field of 10 mT in parallel to the cylinder axis and perpendicular to the magnetic moment of the incident neutron beam was applied. After this, the magnetic field was switched off. Magnetic fields are partially trapped in the superconductor owing to grain boundaries and other defects^{21,22}. The temperature dependence of the residual field distribution inside the sample was visualized by recording radiographic images during step heating from T_0 to T_c with $\Delta T = 0.1$ K. The images (Fig. 3a) show an inhomogeneous residual field that decreases during heating and vanishes completely when the critical temperature T_c is reached at which superconductivity breaks down. For the case (shown in Fig. 3a—7.0 K) of a weak trapped residual field, a tomographic investigation was carried out by rotating the sample around the vertical axis, see Fig. 3b. The measurement consisted of 60 radiographic images recorded at equidistant projection angles over a range of 180°. The beam attenuation for each pixel can be related to equation (1) assuming that the trapped magnetic field conserves its main orientation perpendicular to the beam polarization and is weak enough to cause spin rotations smaller than π for all recorded projections. For the reconstruction of the volumetric data set from the collected two-dimensional images, a numerical reconstruction algorithm (filtered backprojection) was applied²⁴ resulting in a three-dimensional representation of the flux trapped in the sample at 7.0 K (Fig. 3b). Flux concentrations could be found close to the end surfaces of the cylinder and at the position where the sample was held with a screw.

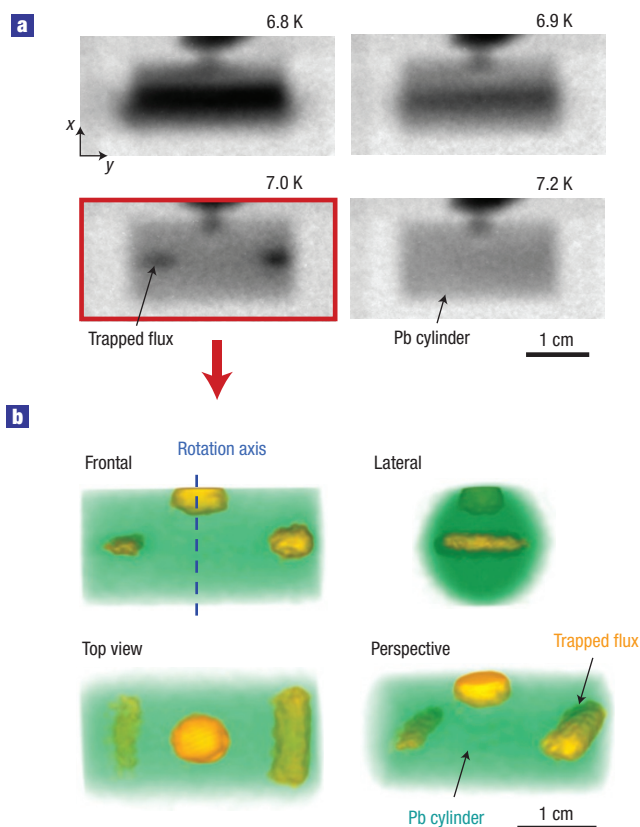


Figure 3 Visualization of magnetic fields with polarized neutrons.

a, Radiographic projections of trapped flux in a polycrystalline lead cylinder at different temperatures below $T_c = 7.2$ K. **b**, Trapped flux at 7.0 K (yellow) visualized in different tomographic views. The magnetic field strength in the sample can be analysed to be about 1.0 ± 0.2 mT (yellow parts, see also Supplementary Information, Fig. S5). This result corresponds well with values observed in the reference coil in Fig. 2, which is of comparable size.

In summary, the introduced method of neutron polarization imaging is superior to conventional techniques because neutrons can penetrate thick layers of matter. For the first time, fields of trapped magnetic flux in a bulk superconductor could be measured, analysed quantitatively and visualized in three dimensions. The method presented is a major step forward not only in the field of neutron imaging but also for investigations of magnetic phenomena in condensed matter. The prospects of imaging with polarized neutrons are not limited to the physics of superconductivity but can also be applied to many other fields of science and technology. For example, effects of bulk magnetism, including magnetic domain distributions in crystals, magnetoelastic and magnetostrictive stress and strains, or even electrical current distributions in conductors (causing, for example, the skin effect) can be addressed. Hence, we predict manifold application of our method in all areas where information about magnetic fields in bulk materials is desirable but currently not available.

METHODS

NEUTRON IMAGING TECHNIQUE

The experiments were conducted at the Hahn–Meitner Institute using the cold neutron radiography facility²⁵. A double-crystal monochromator consisting of two adjustable C(002) crystals with a mosaic spread of 3.5° was used to choose

a wavelength of $\lambda = 0.33$ nm with a bandwidth $\Delta\lambda/\lambda = 0.12$ (ref. 26). The flux density at the sample position for an unpolarized monochromatic beam was about 5×10^5 neutrons $\text{cm}^{-2} \text{s}^{-1}$. The 400- μm -thick scintillator screen used for neutron detection was based on a powder mixture of ^6Li and ZnS providing a maximum light emission at 450 nm wavelength. The light was deflected by a mirror into the 50-mm-focus Nikon camera lens and was recorded by an Andor DW436N-BV CCD (charge-coupled device) camera with $2,048 \times 2,048$ pixels, each $13.5 \times 13.5 \mu\text{m}^2$ in size. The readout time of the chip was $2 \mu\text{s}$ per pixel. The CCD was cooled down to -50°C to minimize electronic noise. The spatial resolution achieved was measured using a test pattern as described elsewhere²⁷. The obtained values were 300 μm in the vertical and 500 μm in the horizontal direction for a sample-to-detector distance of 50 cm. Spatial resolution was lowered by the polarizers and the large sample-to-detector distance and was therefore below the achievable resolution of the instrument of about 100 μm . To enable the investigation of samples wider than the beam width of 15 mm, a scan technique was applied. The samples together with the detector were scanned through the beam defined by the fixed polarizing benders. Exposure times of the order of 15 min were necessary for a single image on a scan path of 6 cm.

NEUTRON POLARIZATION

Both solid-state polarizers used in the experiments consisted of several 250- μm -thick bent Si wafers coated on one side with FeCo polarizing supermirrors and on the other side with Gd (strong neutron absorber). They either deflect or absorb neutrons depending on their spin orientation relative to the magnetic field of two permanent magnets situated on top of and beneath the benders²⁰. The curvature causes a displacement of 250 μm halfway through the polarizer and thus avoids straight and undeflected beam paths. The measured transmission was approximately 30% and the beam cross-section 15 mm \times 40 mm (width \times height). The measured degree of polarization was $\geq 95\%$.

CRYOGENIC TECHNIQUE

For cooling the superconductor, a closed-cycle refrigerator was used that enabled selection of a desired temperature from room temperature down to 5 K with an accuracy of 0.01 K. Magnetic fields were generated by a cylindrical Helmholtz coil.

CALCULATION PROCEDURE

For the comparison presented in Fig. 2, the magnetic field induced by the configuration of current elements with defined strengths and orientations has been calculated as a three-dimensional array using Biot–Savart’s law. The corresponding Larmor precession of the neutron spin was determined recursively voxel by voxel along line trajectories through the field, thus yielding the orientation of the final spin direction relative to the incident polarization. This information was converted to transmission images by assigning grey values between ‘white’ for parallel and ‘black’ for antiparallel spin orientation with respect to the analyser. The calculated image was convoluted with the resolution function of the instrument, an asymmetrical gaussian with a full-width at half-maximum corresponding to the measured resolution in the vertical and horizontal directions. The same procedure was used to compare calculated dipole fields with the measurement presented in Fig. 1. By varying the strength of the dipole field in the calculation, the measured values could be fitted and the whole dipole field could be recovered three-dimensionally (see Supplementary Information, Fig. S3a). The results could also be verified by measuring the magnetic field of 120 ± 5 mT at 4 mm distance from the surface of the dipole (owing to the thickness of the probe and the experimental geometry) using a Hall probe (LakeShore 421 Gaussmeter). The fact that the sample is a dipole as well as the best orientation to simplify the quantification can easily be deduced from various images recorded earlier (see Supplementary Information, Fig. S3).

Received 15 August 2007; accepted 6 February 2008; published 30 March 2008.

References

- Schillinger, B., Lehmann, E. & Vontobel, P. 3D neutron computed tomography: Requirements and applications. *Physica B* **276**, 59–62 (2000).
- Pfeiffer, F. *et al.* Neutron phase imaging and tomography. *Phys. Rev. Lett.* **96**, 215505 (2006).
- Allman, B. E. *et al.* Phase radiography with neutrons. *Nature* **408**, 158–159 (2000).
- Treimer, W. *et al.* Absorption—and phase-based imaging signals for neutron tomography. *Adv. Solid State Phys.* **45**, 407–420 (2005).
- Freeman, M. R. & Choi, B. C. Advances in magnetic microscopy. *Science* **294**, 1484–1488 (2001).
- Zhu, Y. & de Graef, M. *Magnetic Imaging and Its Applications to Materials: Vol. 36 (Experimental Methods in the Physical Sciences)* (Academic, London, 2000).

7. Lake, B. *et al.* Spins in the vortices of a high-temperature superconductor. *Science* **291**, 1759–1762 (2001).
8. Coldea, R. *et al.* Direct measurement of the spin Hamiltonian and observation of condensation of magnons in the 2D frustrated quantum magnet Cs_2CuCl_4 . *Phys. Rev. Lett.* **88**, 137203 (2002).
9. Brandstätter, G. *et al.* Neutron diffraction by the flux line lattice in $\text{YBa}_2\text{Cu}_3\text{O}_{7-\delta}$ single crystals. *J. Appl. Crystallogr.* **30**, 571–574 (1997).
10. de Broglie, L. Waves and quanta. *Nature* **112**, 540 (1923).
11. Rauch, H., Treimer, W. & Bonse, U. Test of a single crystal neutron interferometer. *Phys. Lett. A* **47**, 369–371 (1974).
12. Schlenker, M., Bauspiess, W., Graeff, W., Bonse, U. & Rauch, H. Imaging of ferromagnetic domains by neutron interferometry. *J. Magn. Magn. Mater.* **15–18**, 1507–1509 (1980).
13. Zawisky, M., Bonse, U., Dubus, F., Hradil, Z. & Rehacek, J. Neutron phase contrast tomography on isotope mixtures. *Europhys. Lett.* **68**, 337–343 (2004).
14. Rauch, H. & Werner, S. A. *Neutron Interferometry* (Oxford Univ. Press, Oxford, 2000).
15. Treimer, W., Strobl, M., Hilger, A., Seifert, C. & Feyer-Treimer, U. Refraction as imaging signal for computerized neutron tomography. *Appl. Phys. Lett.* **83**, 398–400 (2003).
16. Williams, W. G. *Polarized Neutrons* (Oxford Univ. Press, Oxford, 1998).
17. Mezei, F. Neutron spin echo: A new concept in polarized thermal neutron technique. *Z. Phys.* **255**, 146–160 (1972).
18. Badurek, G., Hochhold, M. & Leeb, H. Neutron magnetic tomography—A novel technique. *Physica B* **234–236**, 1171–1173 (1997).
19. Jericha, E., Szezywerth, R., Leeb, H. & Badurek, G. Reconstruction techniques for tensorial neutron tomography. *Physica B* **397**, 159–161 (2007).
20. Krist, Th., Kennedy, S. J., Hick, T. J. & Mezei, F. New compact neutron polarizer. *Physica B* **241–243**, 82–85 (1998).
21. Gammel, P. & Bishop, D. Fingerprinting vortices with smoke. *Science* **279**, 410–411 (1998).
22. Jooss, Ch., Albrecht, J., Kuhn, H., Leonhardt, S. & Kronmüller, H. Magneto-optical studies of current distributions in high- T_c superconductors. *Rep. Prog. Phys.* **65**, 651–788 (2002).
23. Johansen, T. H., Bratsberg, H. & Lothe, J. Flux-pinning-induced magnetostriction in cylindrical superconductors. *Supercond. Sci. Technol.* **11**, 1186–1189 (1998).
24. Herman, G. T. *Image Reconstruction from Projections: The Fundamentals of Computerized Tomography* (Academic, New York, 1980).
25. Hilger, A., Kardjilov, N., Strobl, M., Treimer, W. & Banhart, J. The new cold neutron radiography and tomography instrument CONRAD at HMI Berlin. *Physica B* **385–386**, 1213–1215 (2006).
26. Treimer, W., Strobl, M., Kardjilov, N., Hilger, A. & Manke, I. Wavelength tunable device for neutron radiography and tomography. *Appl. Phys. Lett.* **89**, 203504 (2006).
27. Grünzweig, C., Frei, G., Lehmann, E., Kühne, G. & David, C. Highly absorbing gadolinium test device to characterize the performance of neutron imaging detector systems. *Rev. Sci. Instrum.* **78**, 053708 (2007).

Acknowledgements

The authors would like to thank B. Lake for helpful comments and D. Wallacher for experimental support. Correspondence and requests for materials should be addressed to N.K. Supplementary Information accompanies this paper on www.nature.com/naturephysics.

Author contributions

N.K., I.M., M.S. and A.H. contributed equally to this work.

Reprints and permission information is available online at <http://npg.nature.com/reprintsandpermissions/>